Magnetic characterization of non-ideal single-domain monoclinic pyrrhotite and its demagnetization under hydrostatic pressure up to 2 GPa with implications for impact demagnetization

Natalia S. Bezaevaa, Dmitriy A. Chareevd, Pierre Rochette, J. Gattacceca, Myriam Karsf, Jérôme Gattacceca, Joshua M. Feinbergg, Ravil A. Sadykovh, Dilyara M. Kuzinac, Sergey N. Axenovh

HAL Id: hal-01460781

https://amu.hal.science/hal-01460781

Submitted on 24 Feb 2017

Contents lists available at ScienceDirect

Physics of the Earth and Planetary Interiors

Magnetic characterization of non-ideal single-domain monoclinic pyrrhotite and its demagnetization under hydrostatic pressure up to 2 GPa with implications for impact demagnetization

Natalia S. Bezaeva [a,b,c,*], Dmitriy A. Chareev [d,b], Pierre Rochette [e], Myriam Kars [f], Jérôme Gattacceca [e], Joshua M. Feinberg [g], Ravil A. Sadykov [h], Dilyara M. Kuzina [c], Sergey N. Axenov [h]

[a] Faculty of Physics, M.V. Lomonosov Moscow State University, Leninskie Gory, 119991 Moscow, Russia
[b] Ural Federal University, 19 Mira Str., 620002 Ekaterinburg, Russia
[c] Kazan Federal University, 18 Kremlyovskaya Str., 420000 Kazan, Russia
[d] Institute of Experimental Mineralogy, Russian Academy of Sciences, 142432 Chernogolovka, Moscow Region, Russia
[e] Aix-Marseille Université, CNRS, IRD, CEREGE UM34, Technopôle de l'Environnement Arbois-Mediterranée, BP80, 13545 Aix-en-Provence, France
[f] Center for Advanced Marine Core Research, Kochi University, B200 Monobe, Nankoku 783-8502, Japan
[g] Institute for Rock Magnetism, Dept. of Earth Sciences, University of Minnesota, Minneapolis, MN 55455, United States
[h] Institute for Nuclear Research, Russian Academy of Sciences, Prospekt 60-letiya Oktiabria 7a, 117312 Moscow, Russia

A R T I C L E   I N F O

A B S T R A C T

Here we present a comprehensive magnetic characterization of synthesized non-ideal single-domain (SD) monoclinic pyrrhotite (Fe_7S_8). The samples were in the form of a powder and a powder dispersed in epoxy. "Non-ideal" refers to a powder fraction of predominantly SD size with a minor contribution of small pseudo-single-domain grains; such non-ideal SD pyrrhotite was found to be a remanence carrier in several types of meteorites (carbonaceous chondrites, SNC…), which justifies the usage of synthetic compositions as analogous to natural samples. Data were collected from 5 to 633 K and include low-field magnetic susceptibility (χ_0), thermomagnetic curves, major hysteresis loops, back-field remanence demagnetization curves, first-order reversal curves (FORCs), alternating field and pressure demagnetization of saturation isothermal remanent magnetization (SIRM), low temperature data (such as zero-field-cooled and field-cooled remanence datasets together with room temperature SIRM cooling–warming cycles) as well as XRD and Mössbauer spectra. The characteristic Besnus transition is observed at ∼33 K. FORC diagrams indicate interacting SD grains. The application of hydrostatic pressure up to 2 GPa using nonmagnetic high-pressure cells resulted in the demagnetization of the sample by 32–38%. Repeated cycling from 1.8 GPa to atmospheric pressure and back resulted in a total remanence decrease of 44% (after 3 cycles). Pressure demagnetization experiments have important implications for meteorite paleomagnetism and suggest that some published paleointensities of meteorites with non-ideal SD monoclinic pyrrhotite as remanence carrier may be lower limits because shock demagnetization was not accounted for.

© 2016 Elsevier B.V. All rights reserved.

1. Introduction

It is now recognized that the ferrimagnetic iron sulfide Fe_7S_8 known as monoclinic pyrrhotite (4C superstructure) is a mineral of paleomagnetic and rock magnetic significance due to its wide occurrence in a considerable variety of natural environments, terrestrial rocks and meteorites (Arnold, 1967; Sassen et al., 1989; Rochette et al., 1990, 2005; Cournede et al., 2015; Tikoo et al., 2015). Single-domain (SD) pyrrhotite is also a candidate magnetic mineral for the Martian magnetic anomalies (Dunlop and Arkani-Hamed, 2005; Rochette et al., 2005). Additionally, Gilder et al. (2011) discuss pyrrhotite inclusions hosted by diamonds and argue that these inclusions act as geobarometers, preserving information about the pressure conditions under which the diamonds formed in the Earth's mantle.

The magnetic properties of both natural and synthetic pyrrhotites, including their grain-size dependence, have been the subject of several rock magnetic studies (e.g., Clark (1984), Dekkers (1988), Rochette et al. (1990), Menyeh and O'Reilly (1997)). Monoclinic pyrrhotite is characterized by three characteristic transitions. First is the temperature-induced ferrimagnetic-to-paramagnetic phase transition, which occurs upon reaching the Curie temperature ($\sim$593–598 K). Second is the low-temperature magnetic transition or so-called Besnus transition at 30–34 K (Besnus and Meyer, 1964; Rochette et al., 2011). This transition has a crystallographic rather than magnetic origin (Wolfers et al., 2011) and is often used as a diagnostic indicator of the presence of pyrrhotite. Third is the pressure-induced ferrimagnetic-to-paramagnetic transition, which occurs at $\sim$2.8 GPa according to Rochette et al. (2003) and between 1.6 GPa and 6.2 GPa according to Gilder et al. (2011). This pressure-induced transition was the subject of previous studies that employed uniaxial press combined with a solid confining media, resulting in quasi-hydrostatic compression (Rochette et al., 2003; Gilder et al., 2011; note that the neutron experiment in Rochette et al. (2003) was using liquid confining media). It has subsequently been suggested that purely hydrostatic conditions may be a better analog for natural *in situ* conditions in the deep crust (Demory et al., 2013).

Despite these earlier studies characterizing the magnetic properties of natural pyrrhotite, there are still many unanswered questions regarding the mechanisms by which magnetic remanence is acquired by pyrrhotite. How does the underlying crystallography of monoclinic pyrrhotite influence the acquisition of thermal remanence in SD grains? How does the full-vector magnetization of SD monoclinic pyrrhotite change during the Besnus transition? Why are populations of SD pyrrhotite susceptible to gyroscopic remanent magnetization? These magnetic mineralogy questions are best answered using well-characterized synthetic standards, which until this study, have been difficult to obtain as pure phase. Indeed monoclinic pyrrhotite synthesis usually results into a mixture of different sulfides. Here we present a detailed description of the laboratory synthesis and full magnetic characterization of predominantly SD monoclinic pyrrhotite in the 10–633 K temperature range. We compare our data with published results for both natural and synthetic pyrrhotites, and discuss the pressure demagnetization of its saturation isothermal remanent magnetization (SIRM) under hydrostatic pressure up to 2 GPa. This study is meant to lay the groundwork for future research on the magnetic behavior of SD pyrrhotite, and establish a freely available SD pyrrhotite standard that can be used by other research groups in their own studies. Our results also have immediate relevance for the interpretation of Martian crustal magnetic anomalies. Mars shows a pressure gradient of 1.5 GPa per 100 km, and it was previously suggested that the crustal magnetization of Mars is thought to be carried over a thick section of the crust (up to 50 km, see Langlais et al. (2004)) and that peak shock pressure estimates for unmagnetized zones of the Martian crust are of the order of 1–3 GPa (Louzada et al., 2010).

2. Samples and measuring techniques

2.1. Synthesis protocol

Monoclinic pyrrhotite is frequently produced via solid-phase synthesis from elements (Narazawa and Morimoto, 1971; Menyeh and O'Reilly, 1997) or hydrothermally (Kissin and Scott, 1982). Here, we employ an alternative technique: the molten-salt synthesis method (Moh and Taylor, 1971) as it allows synthesized products to achieve equilibrium at much lower temperatures than those used by solid-phase synthesis methods. Relatively low tem-

perature synthesis is necessary to avoid the production of hexagonal rather than monoclinic pyrrhotite. This particular synthesis method also differs from the hydrothermal method in the composition of liquid medium as well as by the use of quartz ampoules instead of autoclaves. In this study monoclinic pyrrhotite was produced in evacuated quartz ampoules using the low-melting eutectic $KCl/AlCl_3$ flux with melting point lower than 427 K (Moh and Taylor, 1971). The starting materials were iron powder Merck (99.5%, 10 μm), crystalline sulfur Johnson Matthey (99.9995%), KCl and anhydrous $AlCl_3$ (Fluka, 98%). Quartz ampoules were heated up to 523–528 K in vertical nongradient tube furnaces over 1–2 h, and then held at this synthesis temperature for three months. Appropriate synthesis temperatures and Fe/S ratios were chosen according to the Fe–S phase diagram (Narazawa and Morimoto, 1971). Sometimes the capsules were taken out of the furnace and shaken to minimize agglomeration. Finally, the ampoules were extracted from the furnace and cooled in air. The mixture of salt and iron sulfide was progressively dissolved first in distilled water, then in alcohol and finally in acetone using an ultrasonic cleaner. The final product was dried in a muffle furnace at 343 K for $\sim$5 min.

Further details on this synthesis procedure can be found in (Chareev et al., 2014), which describes synthesis and investigations of monoclinic pyrrhotite in equilibrium with pyrite (FeS_2) in the Ag–Fe–S system.

To test the reproducibility of the method, we conducted three separate synthesis runs. Representative samples from each of the three synthesis experiments (powder: 'mpo$_1$', 'mpo$_2$', 'mpo$_3$', and powder-in-epoxy: 'mpo$_1^*$'/'mpo$_1^{**}$' (sister samples), 'mpo$_2^*$', 'mpo$_3^*$') all display similar X-ray powder diffraction (XRD) spectra, thermomagnetic analyses, Scanning Electron Microscope (SEM) observations, and hysteresis properties. Thus, the synthesis method appears to be robust and repeatable. The samples 'mpo$_2$' and 'mpo$_3$' were used only for strong-field thermomagnetic curves, XRD and Mössbauer spectra acquisition (see below, Section 2.3).

2.2. Methodology of pressure demagnetization experiments

Pressure demagnetization experiments were carried out on 'mpo$_1^{**}$' powder-in-epoxy sample using two nonmagnetic high-pressure cells of piston–cylinder type allowing direct measurement in a 2G Enterprises SQUID (Superconducting Quantum Interference Device) cryogenic magnetometer allowing for the measurement of moments up to 10^{-4} Am^2 with a practical background noise level of 10^{-11} Am^2. Both cells used in this study have several modifications with regard to the cell described by Sadykov et al. (2008). First, our high-pressure cells were entirely made of "Russian alloy" ($Ni_{57}Cr_{40}Al_3$). Second, their inner diameters were of 8 mm (1st cell) and 7 mm (2nd cell) and the maximum calibrated pressures are 1.8 GPa for the 1st cell and 2 GPa for the 2nd cell. Third, the Teflon plug, described in Sadykov et al. (2008), was replaced in the 1st cell by a special inner piston-plug made of "Russian alloy" with a CuBe antiextrusion gasket (see Sadykov et al. (2008)). The reported (actual) pressure values (e.g., Fig. 9, Table 3) are 10% less with regard to the applied pressures (see Sadykov et al. (2008)). In the 2nd cell both inner pistons were replaced by inner pistons made of cubic boron nitride with Al. We used the following protocol for all pressure demagnetization experiments. After saturation in a 3T magnetic field, the sample was placed into a Teflon capsule, filled with inert polyethylsiloxane (PES-1) liquid and locked with a special piston-plug (first cell) or Teflon plug (second cell). PES-1 allows converting the uniaxial pressure on the pistons into a pure hydrostatic pressure on the sample (Kirichenko et al., 2005).

After loading of the cell with a press (Graseby Specac 15011), pressure inside the cell was fixed. Pressure loading always

occurred within a magnetically shielded room (ambient field ∼ 100 nT). The magnetic moment of the sample under pressure and upon decompression was measured at each pressure step up to 1.8 GPa (1st cell) and up to 2 GPa (2nd cell) using a SQUID magnetometer. The proportion of powder to epoxy in the powder-in-epoxy sister samples mpo$_1^*$ and mpo$_1^{**}$ is circa 1:5 in volume. The powder was stirred inside the resin before solidification to ensure proper dispersion. We assume that the epoxy acts as an isotropic media of higher compressibility and lower friction than pyrrhotite, thus transmitting efficiently the hydrostatic pressure in PES-1 unto the pyrrhotite grains.

The remanence of the 1st empty pressure cell at ambient pressure and room temperature is ∼3·10^{-8} Am^2; at each subsequent pressure step up to 1.8 GPa it was always at least two orders of magnitude lower than the remanence of the investigated sample (so there is no need for correction of the magnetic remanence of the sample by the magnetic remanence of the cell). After decompression the sample was extracted from the cell and demagnetized by AF, then resaturated in a 3T magnetic field and demagnetized by AF again. In this study, median destructive field (MDF$_i$) is defined as the alternating magnetic field needed to reduce a SIRM by half. The first cell was used to complete two pressure runs, one of which included three cycles from ambient pressure to 1.8 GPa and back. The second cell was used to complete two pressure runs up to the maximum pressures of 1.8 GPa and 2 GPa, respectively.

2.3. Methodology of supporting experiments

XRD spectra for the samples 'mpo$_1$' as well as 'mpo$_2$' and 'mpo$_3$' were collected at the Institute of Experimental Mineralogy (IEM), Russian Academy of Sciences (RAS) (Chernogolovka, Russia) using a BRUKER diffractometer with CuKα_1 radiation (graphite monochromator, λ = 1.5406 Å) ('mpo$_1$') and a DRON-7 diffractometer with CoKα radiation (Fe filter, λ = 1.79021 Å) ('mpo$_2$' and 'mpo$_3$'), respectively.

The chemical composition of 'mpo$_1$' was investigated at IEM RAS with a TESCAN Vega II XMU SEM with an integrated energy dispersive microanalysis system INCA Energy 450/XT (20 kV). Backscattered electron images of 'mpo$_1^*$' were taken at the Center for Advanced Marine Core Research, Kochi University (Nankoku, Japan) with a JEOL JSM-6500F SEM. Mössbauer spectra were acquired at room temperature for 'mpo$_2$' and 'mpo$_3$' samples using a Wissel Mössbauer spectrometer with a ^{57}Co source in rhodium matrix and a constant acceleration drive at the Institute of Physics, Kazan Federal University (KFU) (Kazan, Russia). The velocity scale was calibrated using a α-Fe sample.

If not stated otherwise, all magnetic measurements described below were carried out on 'mpo$_1$' and 'mpo$_1^{**}$' samples at CEREGE (Aix-en-Provence, France). All measurements at Kochi University were carried out on 'mpo$_1^*$' sample. Low-field magnetic susceptibility (χ_0) and $\chi_0(T)$ up to 633 K (two subsequent heating–cooling cycles under argon atmosphere) were measured using MFK1-CS3 AGICO apparatus. Anisotropy of magnetic susceptibility (AMS) was quantified for 'mpo$_1^*$' from a separate set of measurements of χ_0 by using a KLY-3 AGICO apparatus at Kochi University. A MFK1-FA AGICO apparatus was used to measure χ_0 frequency (f or F) and field strength (B) dependencies (f_1 = 976 Hz, f_2 = 3904 Hz, f_3 = 15,616 Hz; $B \in [0.003; 0.880]$ mT) on the 'mpo$_1^*$' sample. Table 1 shows two scalar parameters characterizing AMS: the shape parameter T and the degree of anisotropy ratio P.

Strong-field thermomagnetic curves for 'mpo$_2$' and ' mpo$_3$' powder samples were acquired in open air using a custom-made Curie balance (Burov and Yasonov, 1979; Burov et al., 1986) at KFU with a 100 K/min heating rate and a nominal sensitivity of ∼3·10^{-8} Am^2 in 500 mT magnetic field.

The SIRM for 'mpo$_1^{**}$' and its corresponding alternating field (AF) demagnetization spectra was measured using a 2G SQUID magnetometer, equipped with an inline AF demagnetizer. This magnetometer allows for AF demagnetization up to fields of 150 mT. A 3T SIRM was imparted using a pulse magnetizer MMPM9 from Magnetic Measurements Ltd.

Low temperature (5–300 K) magnetic measurements, including zero-field-cooled – field-cooled (ZFC–FC) remanence and room temperature SIRM (RT-SIRM) cooling–warming cycles, were collected using a Quantum Design MPMS-XL5 (Magnetic Property Measurement System) at Kochi University, which has a magnetic moment sensitivity of 10^{-10} Am^2 under applied magnetic fields ranging from 0 to 5 T. The SIRM at 300 K and 5 K was imparted using a 2.5 T magnetic field. The MPMS was also used to measure the field amplitude and frequency dependencies of 'in-phase' (χ') and 'out-of-phase' (χ'') components of χ_0 in the 5–300 K range (F_1 = 1 Hz, F_2 = 10 Hz, F_3 = 100 Hz, F_4 = 997 Hz and B_1 = 25 µT, B_2 = 100 µT, B_3 = 300 µT were used). Finally, the MPMS was also used to collect IRM acquisition curves up to 5 T, and thus, obtain the value of median inductive field (MIF, also referred to as MCF for median constructive field or B'_{cr} for remanent acquisition coercivity), which is the direct magnetic field needed to produce a remanence equal to half of the SIRM.

Major hysteresis loops (with parameters such as saturation magnetization M_s, saturation remanent magnetization M_{rs}, coercivity B_c) and back-field remanence demagnetization curves (with main parameters such as M_{rs} and coercivity of remanence B_{cr}) were measured for all samples at room temperature, using a Princeton Micromag Vibrating Sample Magnetometers (VSM) at CEREGE (with 1T maximum applied magnetic field) and at Kochi University (with 1.5 T maximum applied magnetic field). Acquired hysteresis loops were used to quantify high-field magnetic susceptibility (χ_{hf}), which characterizes paramagnetic as well as diamagnetic and antiferromagnetic contributions. The same type of VSM was used at Kochi University to produce IRM acquisition curve and obtain the value of MIF. The same instruments were also used to conduct first order reversal curve (FORC) measurements for the 'mpo$_1$' and 'mpo$_1^*$' samples. Raw FORC data were processed into FORC distributions using the FORCinel software of Harrison and Feinberg (2008). For 'mpo$_1$' a smoothing factor of 1 was applied. For 'mpo$_1^*$' the VARIFORC protocol of Egli (2013) was used with the following parameters: Sc = Sb = 2.7, Sc1 = Sb1 = 4, lambda = 0.1.

2.4. Description of samples

X-ray powder diffraction data for 'mpo$_1$', 'mpo$_2$' and 'mpo$_2$' are identical; the data were compared against the ICCD/ JCPDS (International Centre for Diffraction Data/ Joint Committee on Powder Diffraction Standards) powder diffraction file database. XRD spectra display two characteristic doublets due to the $(\bar{2}28)/(228)$ and $(\bar{4}08)/408$ reflections. The quadruplet $(\bar{4}08, \bar{2}28, 228, 408)$ is diagnostic of monoclinic pyrrhotite (Chichagov et al., 1990). No trace of hexagonal pyrrhotite was observed, however some pyrite impurity ($\leqslant$10%) is present. SEM-EDS based chemical analyses show that the approximate chemical composition of the 'mpo$_1$' sample was close to Fe$_{1-x}$S with x = 0.125, i.e., Fe$_{0.875}$S or Fe$_7$S$_8$. No impurities of other elements involved in the synthesis procedure (e.g., K, Al, or Cl) were observed.

Observations from SEM photomicrographs (Fig. 1) show that the pyrrhotite particles occur as agglomerates of crystallites, whose individual dimensions are $\leqslant$1–1.5 µm. These grain sizes are slightly too large for dependable estimates of average grain size using the XRD spectra and the Scherrer equation; this method is adapted for samples consisting solely of grains <0.75 µm. Instead, we attempted to roughly estimate the grain size distribution of

Table 1
Rock magnetic properties for "mpo_1-family" samples.

Sample ID	T_c	χ_0	P	T	χ_{hf}	MIF	MDF_i	M_{rs}	M_s	M_{rs}/M_s	B_c	B_{cr}	B_{cr}/B_c
mpo_1	593	30.2	–	–	1.5	–	–	7.9	14.9	0.53	35	41	1.17
mpo_1^*	-	-	1.268	0.799	2.9*	65	–	8.6*	14.9*	0.58	42	51	1.21
mpo_{1p}^{**}	–	–	–	–	1.4*	–	30	8.3*	14.9*	0.56	43	53	1.23

'mpo_1' – Fe_7S_8 powder sample; 'mpo_1^*' and 'mpo_1^{**}' – sister samples of dispersed 'mpo_1' powder in epoxy; 'mpo_{1p}^{**}' is 'mpo_1^{**}' sample after application of 2 GPa. T_c is Curie temperature (in K); χ_0 is low-field magnetic susceptibility (in 10^{-6} m^3/kg); P and T are the degree of anisotropy of magnetic susceptibility (AMS) and AMS shape parameter, respectively; χ_{hf} is high-field magnetic susceptibility (in 10^{-6} m^3/kg); MIF is median inductive field (in mT); MDF_i is median destructive field of SIRM (in mT), SIRM is saturation isothermal remanent magnetization; M_s and M_{rs} are saturation magnetization and saturation remanent magnetization (in Am^2/kg), respectively; B_c is coercivity (in mT), B_{cr} is coercivity of remanence (in mT).
 * These mass normalized values were obtained by deriving pyrrhotite mass assuming fixed M_s.
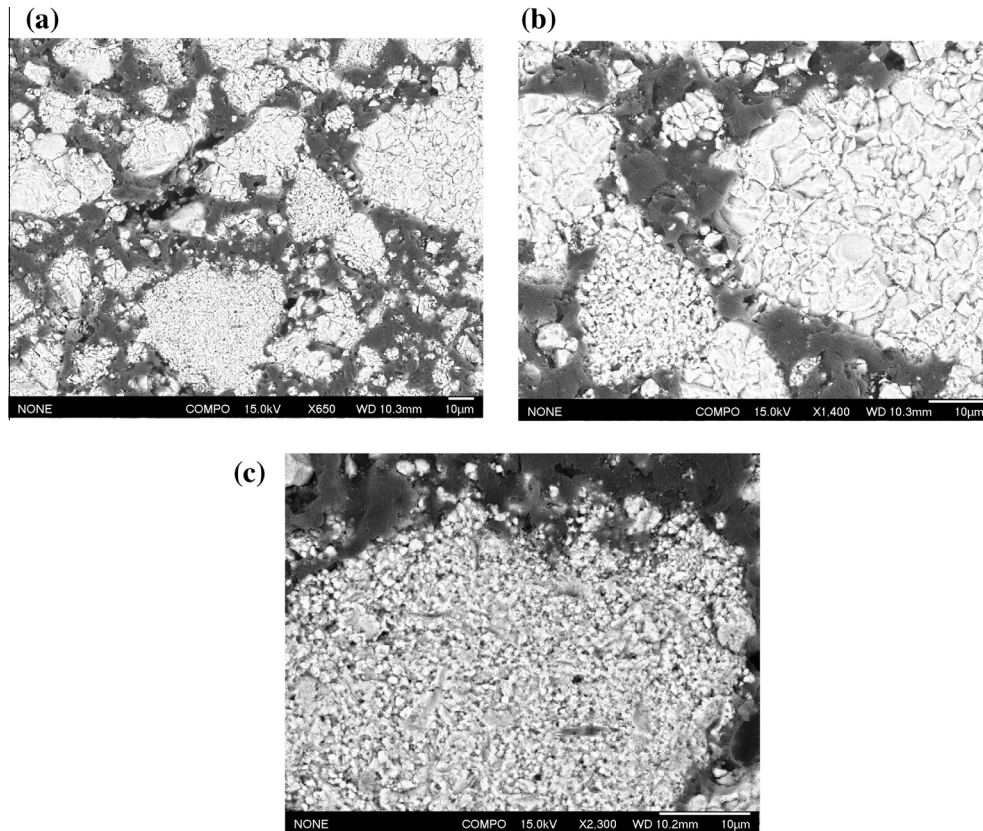
Fig. 1. SEM backscattered electron micrographs of 'mpo_1^*' powder-in-epoxy sample. Epoxy matrix is dark grey. Pyrrhotite grains (light grey) represent the agglomerates of microcrystallites of predominantly 1–1.5 μm size.

our samples using the SEM photomicrographs (Fig. 1). There are two types of agglomerates: coarse-grained (Fig. 1b, the right agglomerate) and fine-grained (Fig. 1b, the agglomerate in the lower left corner and Fig. 1c).

The typical size of aggregates themselves ranges from few microns to 60 μm (Fig. 1a) and the typical sizes of crystallites within coarse-grained and fine-grained aggregates are 1–5 μm and ⩽1.5 μm, respectively. Fine-grained aggregates are far more common than the coarse-grained aggregates. The <1.5 μm grain size of the fine-grained crystallites coincides with the SD magnetic grain size range for pyrrhotite. The single-domain/multidomain (MD) transition grain size for pyrrhotite at room temperature is <2 μm according to experimental estimates of Soffel (1977) for natural pyrrhotite and O'Reilly et al. (2000) for synthetic pyrrhotite and ~3 μm according to calculations of Clark (1984). Thus, while our synthetic samples are likely dominated by SD-like behavior, the SEM micrographs provide evidence for minor contributions of pseudo-single-domain (PSD) grains. For this reason, we refer to our samples as *non-ideal* populations of single-domain grains.

Grains range from equidimensional to highly elongate with a maximum aspect ratio of 1:3. Quantitative examination of 100 grains imaged using Scanning Electron Microscopy shows that the grains have an average width:length ratio of 0.7 ± 0.2.

Fig. 2 shows thermomagnetic curves: two subsequent heating–cooling cycles $M(T)$ (cooling curves not being registered) up to 623 K acquired in open air in 200 mT field for 'mpo_3' (Fig. 2a, the 1st heating curve for 'mpo_2' is coinciding with the presented heating curve) and two subsequent heating–cooling cycles $\chi_0(T)$ up to 633 K acquired in argon for 'mpo_1' (Fig. 2b). The 1st derivatives of the 1st heating curves $M(T)$ (Fig. 2a) and $\chi_0(T)$ (Fig. 2b) reveal a single Curie temperature of ~593 K (320 °C) indicative of monoclinic pyrrhotite. No hexagonal pyrrhotite is observed, as evidenced by the absence of both Curie temperature of hexagonal pyrrhotite (568 K) and its characteristic peak in the 483–523 K temperature range, known as the lambda-transition (antiferromagnetic to ferrimagnetic transition; see Schwarz and Vaughan (1972)). Thus, the observed single Curie point is compatible with XRD and chemical data, all of which point to the successful synthesis of pure monoclinic pyrrhotite. The data
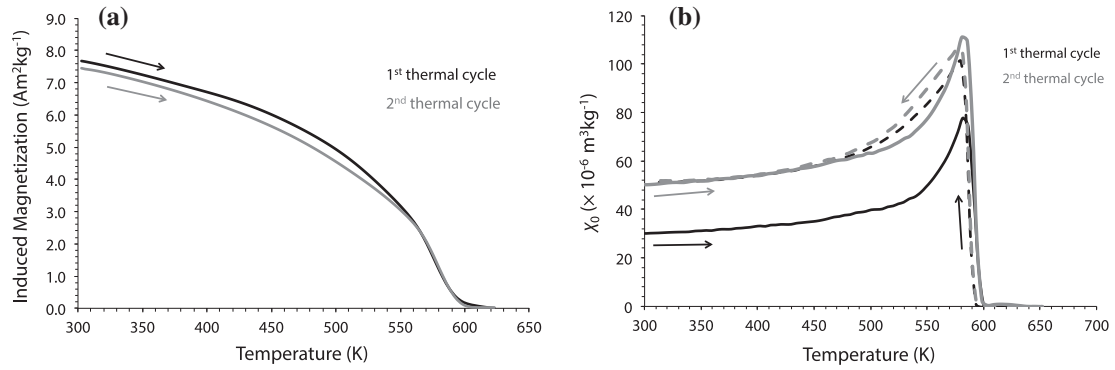
Fig. 2. (a) Strong-field thermomagnetic curves acquired up to 623 K in the 200 mT magnetic field for the 'mpo₃' sample in open air; (b) two consecutive heating–cooling cycles of mass normalized, low-field magnetic susceptibility χ_0 acquired up to 633 K in argon for 'mpo₁' sample. Black lines correspond to the first heating–cooling cycle, whereas gray lines correspond to the second heating–cooling cycle. Solid lines indicate heating cycles and dashed lines indicate cooling cycles (also indicated by the corresponding arrows).

in Fig. 2b also display a well-developed Hopkinson effect, indicative of samples with a significant component of single-domain grains (Dunlop and Özdemir, 1997). It is interesting to note that the strong-field thermomagnetic data shows the room temperature induced magnetization decreasing by ∼3% after the 1st thermal cycling, whereas the room temperature, mass normalized susceptibility increases by nearly 100% after the first thermal cycling (and is essentially reversible during the second thermal cycling). The relatively minor decrease in induced magnetization suggests that, in spite of heating in open air, there was little mineralogical alteration during the strong-field experiment, but the two-fold increase in susceptibility suggests that some grain size coarsening may have occurred during the initial heating and cooling cycle. Alternatively, we may interpret the susceptibility increases as a temperature-induced relaxation of anisotropy related to residual stress and crystallographic defects.

Fig. 2a and further thermal cycling indicate reliable thermal stability of the material after initial heating and cooling cycle. Indeed, further subsequent in-field thermal cycles (double heating–cooling cycles up to 673 K, 723 K, 773 K, 873 K, 923 K and 973 K acquired after the 1st double thermal cycle up to 623 K) showed that the induced magnetization decreased only by 7% after four single thermal cycles in open air (up to maximum temperature of 673 K) and each of four heating curves is characterized by a single Curie temperature of monoclinic pyrrhotite. The decrease in induced magnetization may be due to conversion of monoclinic pyrrhotite

into hexagonal pyrrhotite during heating, although no lambda-transition was observed on either of the thermomagnetic curves, indicating only a negligible quantity of hexagonal pyrrhotite (if any). Visible oxidation of monoclinic pyrrhotite and further formation of magnetite started to occur only after the 5th thermal cycle (to maximum temperature of 723 K) and was followed by an increase in induced magnetization. Indeed, the breakdown of pyrrhotite into magnetite was previously shown to result in a large irreversible increase in induced magnetization (Dekkers, 1990). Further breakdown of magnetite into hematite results in irreversible drastic decrease in induced magnetization.

Fig. 3 shows the experimental and fitted Mössbauer spectra for 'mpo₃'. The spectrum of 'mpo₃' sample is fitted with four magnetic sextets (monoclinic pyrrhotite) and one paramagnetic doublet (pyrite) and corresponding fitting parameters are listed in Table 2. The spectrum (Fig. 3) has a typical pattern of monoclinic pyrrhotite (Gosselin et al., 1975; Gilder et al., 2011) with pyrite (Evans et al., 1982) and isomer shift values for all subspectra (Table 2) are compatible with Fe_7S_8 (Gosselin et al., 1975) and pyrite (Evans et al., 1982). The impurity of pyrite represents about 10 mol.%.

3. Experimental results

3.1. Rock magnetic properties of the samples

Main rock magnetic properties of our synthetic samples are summarized in Table 1. Raw and slope-corrected hysteresis loops are presented in Fig. 4. Hysteresis loops exhibit SD behaviour (e.g., Gilder et al. (2011)) with remanence ratios M_{rs}/M_s = 0.53 (powder sample 'mpo₁') and 0.58 (dispersed powder sample 'mpo₁*') and the coercivity ratios B_{cr}/B_c = 1.17 ('mpo₁') and 1.21 ('mpo₁*'). The remanence and coercivity ratios for both samples are slightly different due to setting the powder 'mpo₁' into epoxy (samples 'mpo₁*' and 'mpo₁**'), which decreases the extent of magnetostatic interactions between neighboring grains in the dispersed sample
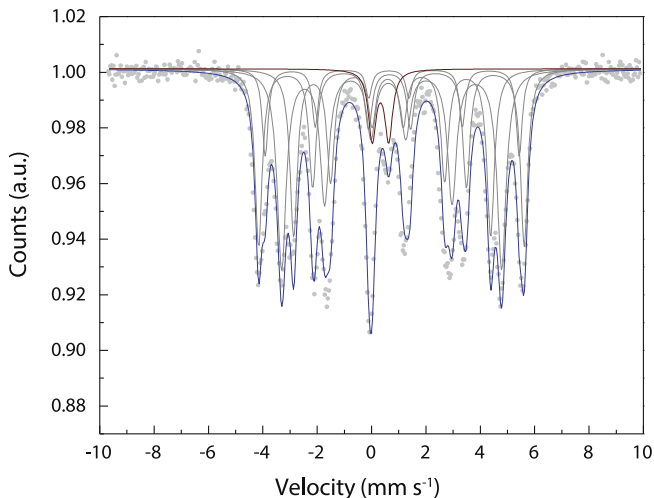
Fig. 3. Mössbauer spectrum of 'mpo₃', recorded at room temperature (see Table 2 for fitting parameters). "a.u." is for arbitrary units.

Table 2
Mössbauer parameters for mpo_3 sample at room temperature.

| Sample ID	HF	IS	Relative areas (%)
mpo₃	22.5	0.68	23
	25.2	0.68	33
	29.1	0.70	10
	30.4	0.70	24
	0.0	*0.33*	*10*

HF is hyperfine field (in T); IS is isomer shift (in mm s⁻¹). Mössbauer parameters corresponding to paramagnetic doublet (pyrite) are italized.

Table 3
Overview of hydrostatic pressure demagnetization experiments on pyrrhotite-bearing samples up to 1.2 GPa (Bezaeva et al., 2007, 2010) and up to 1.8 GPa (this study).

Sample ID	B_{cr}	Domain state	$\Delta_{1.2\,GPa}$	$\Delta_{1.8\,GPa}$	DHP10%	DHP20%
NWA1068	134	Near SD	16	*25*	0.93	*1.48*
NWA753	134	PSD	10	*15*	1.24	*2.30*
sb3a	31	PSD	22	*36*	0.62	1.18
127037	7	MD	20	*33*	0.80	1.24
pyr-a,b	17–23	MD	27–29	*34–37*	0.18–0.26	0.49–0.77
mpo$_1^{**}$	51	Non-ideal SD	30	38	0.27	0.63

B_{cr} is coercivity of remanence (mT); SD, PSD and MD are for single-domain, pseudo-single-domain and multidomain, respectively; $\Delta_{1.2\,GPa}$ and $\Delta_{1.8\,GPa}$ are pressure demagnetization degrees under hydrostatic loads of 1.2 GPa and 1.8 GPa, respectively. DHP10% and DHP20% are destructive hydrostatic pressure values, which lead to 10% and 20% of SIRM demagnetization, respectively. SIRM – saturation isothermal remanent magnetization, acquired in 3T magnetic field. $\Delta_{1.8\,GPa}$ and DHP20% values are italized when estimated based on linear trend plotted on the basis of last three pressure steps (0.93, 1.08 and 1.24 GPa) from corresponding pressure demagnetization curve up to 1.24 GPa (see Bezaeva et al. (2007, 2010)).
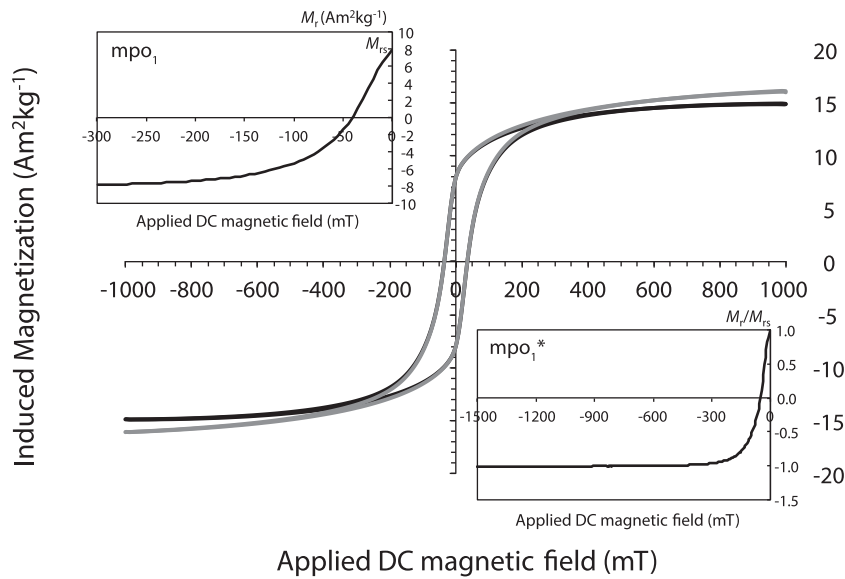
Fig. 4. Raw (grey curve) and slope-corrected (black curve) hysteresis loops acquired for 'mpo$_1$' sample. Insets: backfield remanence demagnetization curves acquired for the powder sample 'mpo$_1$' (upper left inset) and powder-in-epoxy sample 'mpo$_1^*$' (lower right inset). "*DC*" is for direct current.

leading to a slightly higher remanence ratio. Menyeh and O'Reilly (1996) also found the same value of M_{rs}/M_s (0.55) for their SD synthetic pyrrhotite with crushed grain fraction < 1 μm. Bulk coercivity B_c values are 35 mT ('mpo$_1$') and 42 mT ('mpo$_1^*$') (Table 1).

All mass normalized values provided below correspond to 'mpo$_1$' sample. In case of 'mpo$_1^*$' and 'mpo$_1^{**}$' samples there was no way to normalize the data by volume or mass due to the type of used samples (powder-in-epoxy). Therefore, we derived sample mass based on the M_s measured on the pure powder. Saturation magnetization M_s is 14.9 Am^2/kg, which agrees well with published data on monoclinic pyrrhotite (Dekkers, 1988), taking into account the circa 10% proportion of non-magnetic pyrite.

Backfield remanence demagnetization curves acquired up to 300 mT ('mpo$_1$') and 1500 mT ('mpo$_1^*$') are presented in Fig. 4 (see insets). Corresponding bulk coercivity of remanence B_{cr} values are 41 mT ('mpo$_1$') and 51 mT ('mpo$_1^*$'). In order to check for anisotropy level of powder-in-epoxy samples, we measured hysteresis loops and backfield curves for mpo$_1^*$ and mpo$_{1p}^{**}$ in three perpendicular directions. The samples are rather isotropic. Indeed, the changes in B_{cr}, B_c, M_{rs}/M_s, B_{cr}/B_c are negligible (<1–3%) and the changes in M_{rs} and M_s are within 4–12%.

Fig. 5 displays the IRM acquisition curves acquired up to 1.5 T (Princeton VSM) and up to 4.4 T (MPMS). MIF values obtained from both curves are 65 mT and 73 mT; we will further refer to

the 1st value (Table 1), as it is more precise due to the smaller field steps used in the VSM-based IRM acquisition experiment.

First-order reversal curve (FORC) distribution (Fig. 6) provides information about the distribution of microscopic coercivities within a sample and the magnetic interactions within magnetic mineral assemblages (Roberts et al., 2000).

Room-temperature FORC diagrams for 'mpo$_1$' (Fig. 6a) and 'mpo$_1^*$' (Fig. 6b) samples are typical of interacting SD grains (Roberts et al., 2000). There is no evidence of superparamagnetic (SP) grains as would be suggested by a secondary peak near the origin of the plot, and only minor evidence of PSD behavior (Roberts et al., 2000). Our FORC diagrams (Fig. 6) share broad similarities with the FORC diagram obtained by Wehland et al. (2005) for the finest dispersed powder of grain-sized monoclinic pyrrhotite with grain size <5 μm (see Fig. 1 in (Wehland et al., 2005)). The distribution of interactions shown for both the powder and powder-in-epoxy samples are most likely due to magnetostatic clumping of the grains, as well as interactions inherent to PSD grains. To get a perspective on the distribution of microcoercivities in each sample, without the influence of interactions, we show marginal coercivity distributions for 'mpo$_1$' (Fig. 6c) and 'mpo$_1^*$' (Fig. 6d). Fig. 6a-d show that both 'mpo$_1$' and 'mpo$_1^*$' contain grains with microcoercivities > 100 mT.
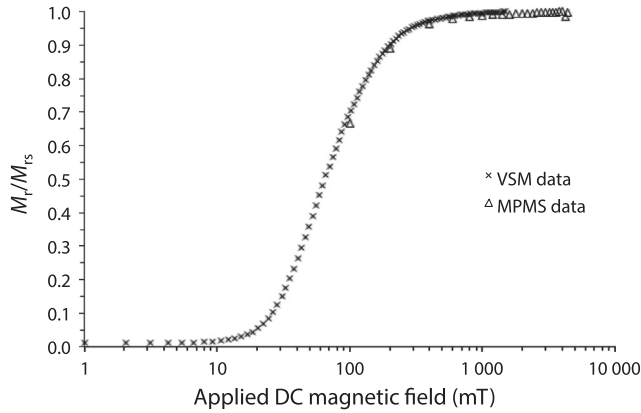
Fig. 5. IRM acquisition curves acquired for 'mpo$_1^*$' sample up to 1500 mT using Princeton VSM and up to 4400 mT using MPMS. IRM is normalized to its maximum value (SIRM) as there is no way to normalize it by volume or mass due to the type of the sample – powder-in-epoxy. M_r is remanent magnetization, M_{rs} – saturation remanent magnetization; "DC" is for direct current.

MDF$_i$ of SIRM is 30 mT (sample 'mpo$_1^{**}$', see Table 1) and MIF/MDF ratio is 2.2. This indicates an asymmetry in the magnetization and demagnetization processes (O'Reilly et al., 2000).

3.2. Low-temperature magnetic (Besnus) transition

Fig. 7 displays RT-SIRM cooling–warming cycles (Fig. 7a) as well as ZFC-FC data (Fig. 7b). The Besnus transition of monoclinic pyr-

rhotite is visible on all four curves (see Fig. 7). However Rochette et al. (1990) pointed out that RT-SIRM cooling curve is the most appropriate to pinpoint the Besnus transition: it occurs in our case at ~ 33 K (as estimated from the maximum on the 1st derivative of the RT-SIRM cooling curve), after which there is sharp decrease in magnetization observed (Fig. 7a) consistent with literature (Rochette et al., 1990). These data are also consistent with recent 3-axis measurements of the Besnus transition collected on a single crystal of pyrrhotite using a low temperature insert at the Institute for Rock Magnetism at the University of Minnesota (Feinberg et al., 2015). There is no suggestion of SP grains in Fig. 7b, because SIRM at 5 K between FC and ZFC differs by less than 3% (Bowles et al., 2009), although, the presence of SP grains is more accurately determined using the frequency dependence of magnetic susceptibility.

3.3. Magnetic susceptibility and its field amplitude and frequency dependencies

Room-temperature low-field magnetic susceptibility χ_0 of mpo$_1$ sample is $30\cdot10^{-6}$ m^3/kg (Table 1), consistent with literature (Dekkers, 1988). $\chi_0(T)$ heating–cooling cycles up to 633 K and strong-field thermomagnetic curves up to 623 K were discussed above (Fig. 2, subsection 2.4). AMS measurements on 'mpo$_1^*$' sample revealed the oblate shape of AMS ellipsoid (with AMS shape parameter $T \sim 0.8$, see Table 1) and the degree of anisotropy of χ_0 of 27% (P-parameter, see Table 1). In view of the remanence anisotropy data presented in subsection 3.1, which showed that our powder-in-epoxy samples are rather isotropic, it is unlikely that
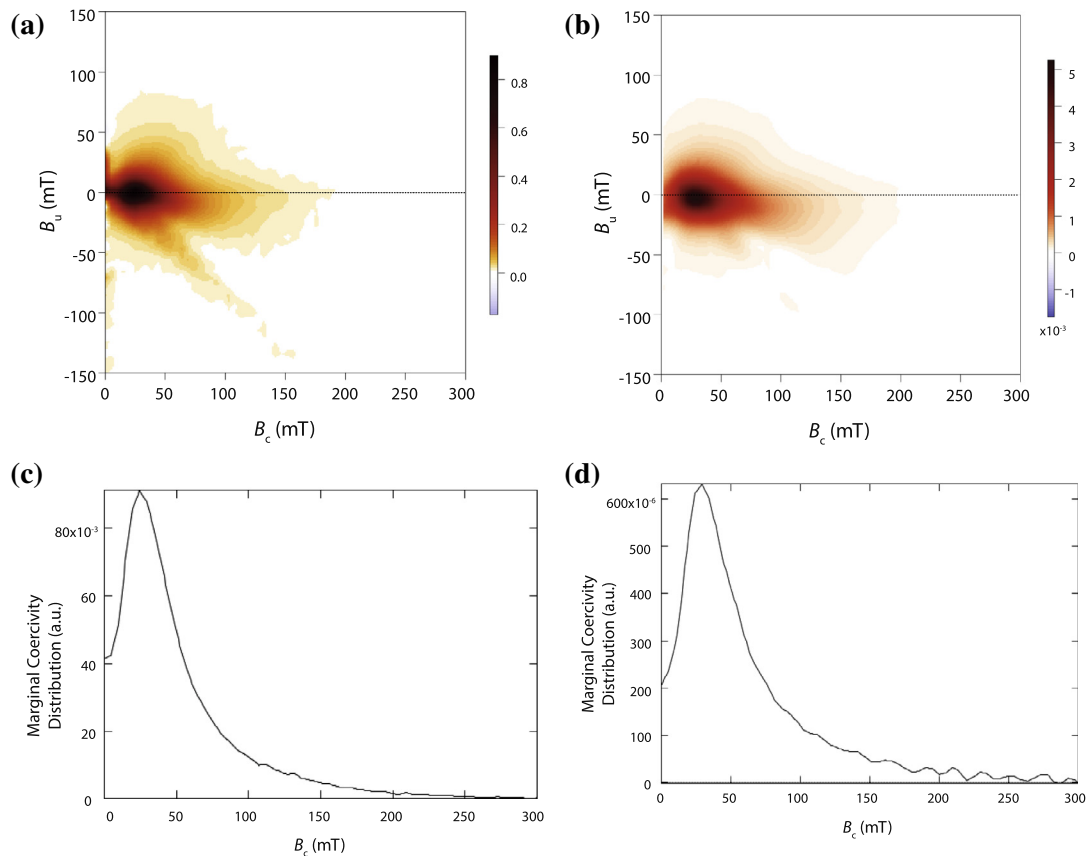
Fig. 6. FORC (first-order reversal curve) diagrams for (a) 'mpo$_1$' powder sample and (b) 'mpo$_1^*$' powder-in-epoxy sample, collected at room temperature. A sample's distribution of microcoercivities, regardless of interactions, is called the 'marginal coercivity distribution' and is shown for each sample in (c) and (d). The distribution of microcoercivities exceeds 100 mT for both 'mpo$_1$' and 'mpo$_1^*$', which is consistent with a population of interacting single-domain grains. FORC data were processed using FORCinel (Harrison and Feinberg, 2008). "a.u." is for arbitrary units.
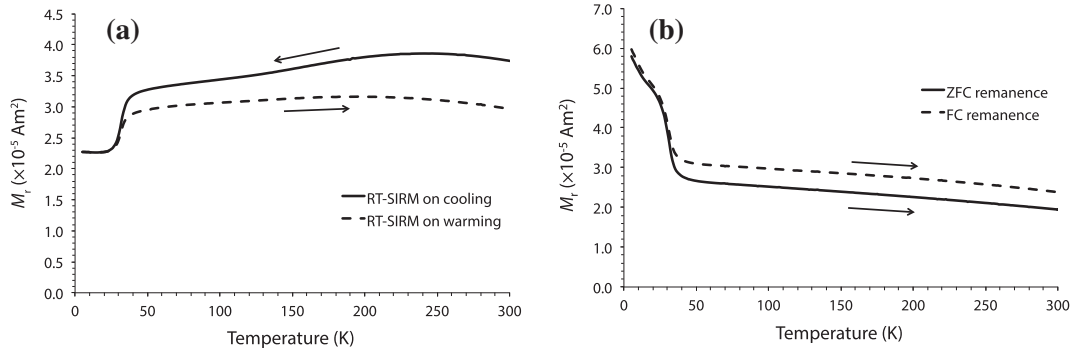
Fig. 7. (a) Room temperature saturation isothermal remanent magnetization (RT-SIRM) on cooling (solid line) and on warming (dashed line) in the 5–300 K temperature range versus temperature for 'mpo₁*'; (b) ZFC (zero-field-cooled) - FC (field-cooled) remanence data set for 'mpo₁' sample. Solid line shows zero-field warming of a remanence acquired isothermally in a 2.5 T magnetic field at 5 K after zero-field cooling from 300 K; dashed line shows a zero-field warming of a remanence acquired by field cooling from 300 K in a 2.5 T magnetic field; the Besnus transition occurs at approximately 33 K; the Besnus transition temperature was estimated as the maximum of the 1st derivative on the RT-SIRM cooling curve as suggested by Rochette et al. (1990).
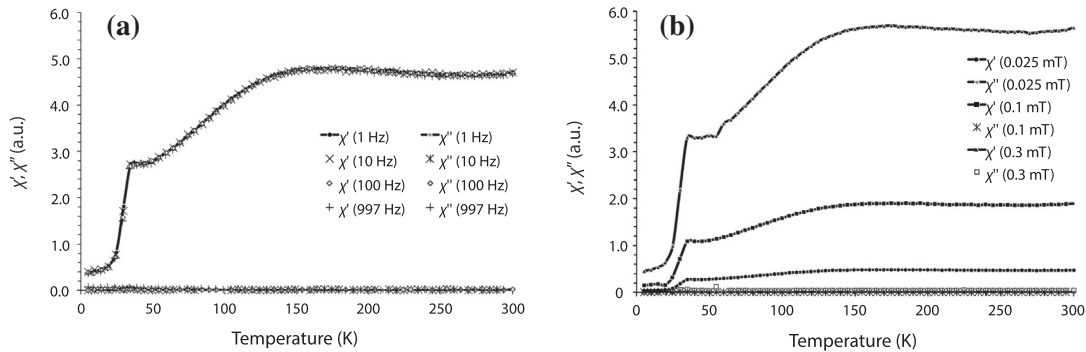
Fig. 8. 'In-phase' χ' and 'out-of-phase' χ'' components of magnetic susceptibility χ_0 of 'mpo₁*' versus temperature in the 5–300 K temperature range at different frequencies F and field amplitudes B. (a) F_1 = 1 Hz, F_2 = 10 Hz, F_3 = 100 Hz, F_4 = 997 Hz; B = 0.025 mT; (b) F = 1 Hz, B_1 = 0.025 mT, B_2 = 0.1 mT and B_3 = 0.3 mT. "a.u." is for arbitrary units.

such high P value may be considered as reliable. Indeed, the powder-in-epoxy sample used for AMS measurements is rather small ($\sim[4 \times 4 \times 2]$ mm, irregular shape) to provide a reliable AMS dataset.

Fig. 8 shows 'in-phase' χ' and 'out-of-phase' χ'' components of magnetic susceptibility χ_0 versus temperature from 5 to 300 K as a function of frequency F and AC (alternating current) magnetic field amplitude B, measured in order to check the presence of SP fraction and to double-check the grain size in the synthesized pyrrhotite samples (see below). The Besnus transition is directly visible on all $\chi'(T)$ curves at about 30-34 K (Fig. 8, see the sharp decrease in χ' below 34 K).

As illustrated in Fig. 8a for B = 0.025 mT, at 300 K, χ' differs by $\leqslant 0.8\%$ in the 1 to 997 Hz frequency range. Thus, there is no frequency dependence of χ' or χ'' observed over all the temperature range for the used frequency range (1–997 Hz), which holds for all other B values as well (i.e., 0.1 and 0.3 mT). Moreover, χ'' is always at least two orders of magnitude lower than its corresponding χ' value and thus negligible at all temperature range for all B and F values. This represents an independent confirmation for the negligible contribution of SP grains to the magnetic properties of our samples (the SP threshold for monoclinic pyrrhotite is ~ 0.017 µm (Clark, 1984)). Fig. 8b displays field dependence of χ' and χ'' for F = 1 Hz, where χ' is observed to covary with B. Indeed, χ' increases by one order of magnitude from B = 0.025 mT to B = 0.3 mT for F = 1 Hz. The same (rather strong) field dependence is observed for other frequencies (10 Hz, 100 Hz), which suggests the presence of grains bigger than stable

SD (Worm et al., 1993), an idea which is supported by SEM imagery showing a minor component of PSD grains.

Room-temperature frequency and field dependencies of χ_0 were measured for higher field amplitudes (up to 0.880 mT) and frequencies (up to $\sim$ 15 kHz). The general tendency of frequency-independent χ_0 holds up to 15,616 Hz. There is no field dependence observed in the 976 Hz to 15 kHz frequency range. This is consistent with published $\chi'(f, H)$ data for pyrrhotite (Worm et al., 1993), where authors observe practically constant behavior of χ' in the 0.01 to 2 mT field range for f = 2 kHz and grain-sized samples with sizes < 5 µm, 15 µm and 20 µm.

3.4. Pressure demagnetization

We conducted several pressure demagnetization runs on the 'mpo₁**' powder-in-epoxy sample up to 1.8 GPa and one run up to 2.0 GPa. Fig. 9a displays IRM under pressure (normalized to its zero-pressure SIRM) versus hydrostatic pressure up to 1.8–2.0 GPa.

The first three 0 to 1.8 GPa (independent) pressure experiments and the first 0 to 2 GPa pressure cycle all resulted in 32 to 38% demagnetization of initial SIRM. The same degree of demagnetization occurs regardless of whether the 1st or the 2nd pressure cell was used. Repeated cycling resulted in further decrease in remanence and total demagnetization after three consecutive pressure cycles of 44% (Fig. 9b), although each successive pressure cycling led to smaller net changes in magnetization. Decompression from 1.8 GPa to ambient pressure always results in further 16 to 19% increase in residual magnetic remanence. This remanence increase,
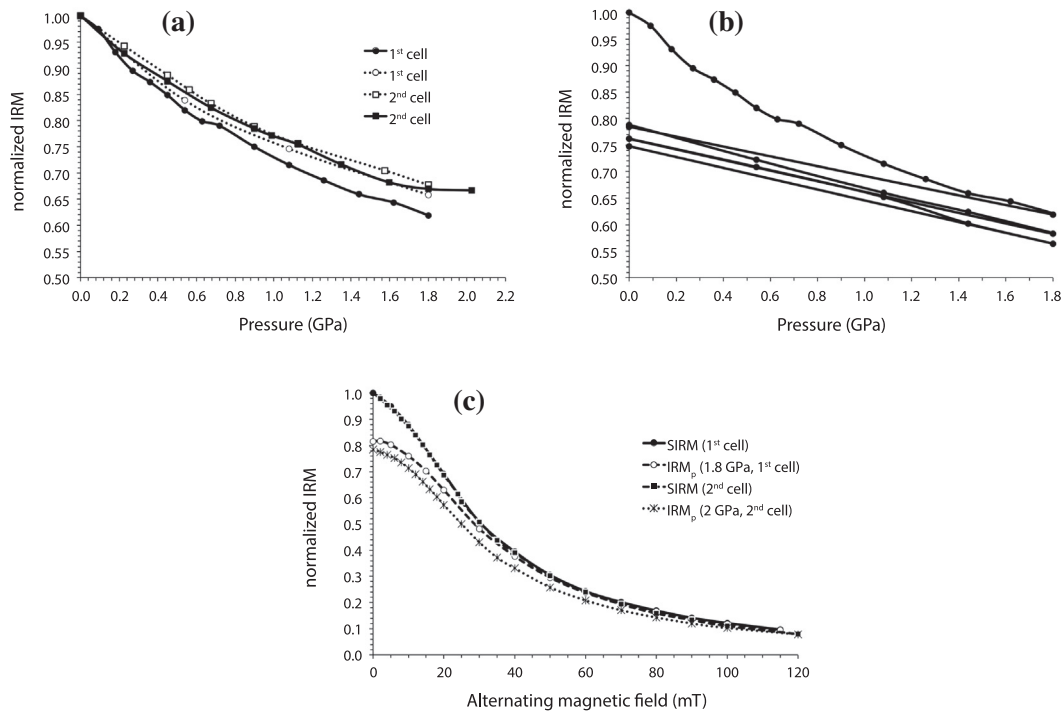
Fig. 9. (a) Independent 0–1.8 GPa and 0–2 GPa pressure runs for the 'mpo$_1^{**}$' powder-in-epoxy sample: residual isothermal remanent magnetization under pressure (normalized to its initial ambient pressure SIRM) versus hydrostatic pressure up to 1.8 GPa and 2 GPa; (b) three consecutive pressure cycles from ambient pressure to 1.8 GPa and back; (c) Alternating field (AF) demagnetization of SIRM and residual isothermal remanent magnetization IRM$_p$ upon decompression from 1.8 GPa and from 2 GPa (AF demagnetization of SIRM was performed prior to corresponding pressure demagnetization experiments). All values are normalized by room-pressure SIRM, measured at room temperature. All indicated pressure values were corrected for 10% and correspond to real pressure values (see Subsection 2.2).

which was also observed upon decompression from 2 GPa (15% increase), is typical behavior for pyrrhotite upon decompression (Bezaeva et al., 2010).

AF demagnetization curves of SIRM and residual IRM after pressure release (IRM$_p$) are presented in Fig. 9c. As follows from Fig. 9c, pressure demagnetization mainly affects the lower coercivity component of the mineral assemblage as was previously proposed by Bezaeva et al. (2010).

However, it is clear from Fig. 9c that demagnetization by higher pressure (2 GPa versus 1.8 GPa) also affects the higher coercivity portion of the assemblage, as the AF demagnetization curve of IRM$_p$ after decompression from 2 GPa lies below the corresponding IRM$_p$ curve after decompression from 1.8 GPa. The coercivity spectra observed during these AF demagnetization spectra are consistent with the microcoercivity distributions observed in the FORC data. The MDFs in Fig. 9c range from 25 to 30 mT, which is consistent with the median peak values observed in the marginal coercivity distributions for the FORC data (Fig. 6c-d). Similarly, the AF demagnetization spectra show a population of high coercivity grains extending out to 120 mT, similar to the extent of high coercivity grains observed in the FORC distributions.

We have not observed any permanent pressure-induced changes in SIRM (within 4% window), which is consistent with the conclusions of Gilder et al. (2011) that magnetic remanence in SD pyrrhotite is largely insensitive to pressure until 2 GPa. There are no pressure-induced changes observed in B_{cr} (reflecting the magnetic hardness of the sample) nor hysteresis parameters (M_{rs}/M_s, B_c, B_{cr}/B_c) upon decompression from 2 GPa. This indicates that no permanent changes in hysteresis properties took place during pressure cycling, which is consistent with Bezaeva et al. (2010) and Demory et al. (2013) and at odds with Gilder et al. (2011). This difference might come from a higher pressure applied by Gilder et al. (2011) (3 GPa for SD sample) as well as from differences in

the pressure environments between our study (purely hydrostatic compression) and that of Gilder et al. (2011); quasi-hydrostatic compression but with significant deviatoric stress).

4. Discussion

4.1. Grain size

Several lines of evidence indicate that our synthetic samples are dominated by SD grains, with minor contributions from PSD grains. As indicated in subsection 3.1, the bulk coercivity values B_c (35 mT for 'mpo$_1$' powder sample and 42 mT for 'mpo$_1^*$' dispersed powder sample, Table 1) are broadly consistent with the median microcoercivities observed in the FORC diagrams, which also show a smaller population of high coercivity grains with switching fields > 100 mT (Fig. 6a-d). We interpret this range of coercivities as evidence for a range of grain sizes. Electron micrographs also show a range of grain sizes that are compatible with this model. Indeed, in spite of comparative values of M_{rs}/M_s ratio (0.55) and room temperature χ_0 ($30 \cdot 10^{-6}$ m^3/kg) (also consistent with Dekkers (1988)), Menyeh and O'Reilly (1996) observed higher values of MDF$_i$ (53 mT) and B_c (78 mT), B_{cr} (101 mT) and M_s (18.3 ± 0.3 Am^2/kg) for their pure SD samples with grain size < 1 μm than those indicated in Table 1. However, Menyeh and O'Reilly (1996) used crushed samples, and it is known that the crushing procedure induces strain anisotropy, which results in elevated B_c and B_{cr} values. This may explain why MDF$_i$, B_c, B_{cr} and M_s values for our samples (Table 1) are slightly lower that those found by Menyeh and O'Reilly (1996) for their pure SD samples.

As indicated in Subsection 2.4, the pyrrhotite crystallites in this study are predominantly 1–2 μm-sized (Fig. 1); though grains up to 5 μm are also observed (Fig. 1), the latter corresponding to PSD grain size range (Dekkers, 1988). However, Menyeh and

O'Reilly (1996) argue that grain size, which controls the magnetic domain state of grains is not equivalent to electron-optical grain size due to the failure of SEM to distinguish between individual grains and clusters of fine particles. Menyeh and O'Reilly (1996) found the magnetic grain size for their samples to be ten times smaller than mean electron-optical grain size.

In fact, it is known that M_{rs}/M_s, B_{cr} and B_c decrease with increasing grain size (Dekkers, 1988). Our observed B_c and M_{rs}/M_s values (B_c = 35 mT and 42 mT; M_{rs}/M_s = 0.53 and 0.58, see Table 1) are higher if compared to what was previously reported for PSD-ranged monoclinic pyrrhotite. Indeed, Menyeh and O'Reilly (1997) reported the following hysteresis parameters for crushed undifferentiated monoclinic pyrrhotite with 1–50 μm grain size range: B_c = 30 mT and M_{rs}/M_s = 0.386. Soffel (1981) reported that for his pyrrhotite-bearing diabase samples saturation remanence is about half of saturation magnetization and B_c = 18 mT indicate the presence of grains with SD and PSD behavior.

The pyrrhotite grain size distribution for our samples can also be estimated from the value of remanent coercivity B_{cr} (as suggested by Dekkers (1988), see Table 4 in (Dekkers, 1988)). This estimate gives a range of 15–40 μm. B_{cr}-based estimates from the data of Clark (1984) yield a range of 20–32 μm and from data of Menyeh and O'Reilly (1997) give a range of 5–23 μm (see Table 1 in Menyeh and O'Reilly (1997)). The absence of field dependence of room-temperature χ_0 at $f \sim 15$ kHz reveals grain size $\leqslant 20$ μm (see Fig. 6 in (Worm et al., 1993), which displays χ' versus B for grain-sized monoclinic pyrrhotite samples within 5–250 μm range for f = 2 kHz). Thus, all estimates of grain size in our samples from rock magnetic parameters consistently indicate PSD grain size range. It was shown by Menyeh and O'Reilly (1998) that synthetic monoclinic pyrrhotite particles of 1–2 μm and 26–29 μm typically contain two and five domains, respectively. However, previous authors (e.g. Menyeh and O'Reilly (1997), Dekkers (1988)) used crushed samples with impurities of hexagonal pyrrhotite, all of which may artificially increase B_{cr} and bias B_{cr}-based grain size estimation for pure monoclinic pyrrhotite.

Thus, direct SEM observations of numerous crystallites of $\leqslant 1$–2 μm, FORC diagrams (Fig. 6) and the discussion above allow us to conclude that our material is predominantly characterized by SD grains, however, to a smaller extent, our materials are likely to also contain small PSD grains containing a few domains. In such instances, bulk hysteresis parameters will represent the average magnetic properties between SD and PSD grains, and for this reason, we refer to such populations as «non-ideal SD monoclinic pyrrhotite».

The observed B_{cr}, B_c and MIF (Table 1, sample 'mpo$_1^*$') values match those suggested by Clark (1984) for monoclinic pyrrhotite, i.e., MDF$_i$ < B_{cr} < MIF. They are related (within 5% incertainty) according to the empirical equation B_{cr} = $(B_c$ + MIF)/2, found by O'Reilly et al. (2000) for synthetic pyrrhotite of 1–20 μm fraction size.

4.2. Pressure demagnetization experiments

The SIRM of pure monoclinic pyrrhotite Fe$_7$S$_8$ is pressure-sensitive and exhibits a pressure demagnetization of 32 to 38% under hydrostatic loads of 1.8–2 GPa. Table 3 displays an overview of results from our current pressure demagnetization experiments up to 1.8 GPa together with results from previous hydrostatic pressure demagnetization experiments up to 1.2 GPa (Bezaeva et al., 2007, 2010) such as pressure demagnetization degree $\Delta_{1.2 \text{ GPa}}$ (%) under 1.2 GPa, estimated potential $\Delta_{1.8 \text{ GPa}}$ (%) under 1.8 GPa of hydrostatic load (on the basis of last three pressure steps of 0.98, 1.02 and 1.24 GPa and under the assumption of further linear behaviour of pressure demagnetization curve; such estimation reveals the upper limit of potential $\Delta_{1.8 \text{ GPa}}$) and B_{cr} for the following pyrrhotite-bearing samples: near SD NWA1068 Martian meteorite, PSD NWA753 Rumuruti chondrite, PSD schist, 127037 MD pyrrhotite polycrystal (Louzada et al., 2010), MD dispersed powder of monoclinic pyrrhotite (two samples). As seen from Table 3, 'mpo$_1^{**}$' is the most pressure sensitive sample: it exhibits the highest pressure demagnetization of all investigated samples. It was previously shown by Bezaeva et al. (2010) for 1.2 GPa that the degree of pressure demagnetization is roughly proportional to ln(B_{cr}). This also holds for 1.8 GPa. Indeed, our data and estimates for 1.8 GPa roughly fit into equation: IRM$_p$/SIRM [%] = 0.05·ln(B_{cr}) + 0.51 (where IRM$_p$/SIRM = 1 − $\Delta_{1.8}$). This empirical equation can be further used to roughly estimate the potential pressure demagnetization degree of pyrrhotite-bearing samples under hydrostatic pressure of 1.8 GPa from its B_{cr} value (in mT).

Most of the pyrrhotite-bearing samples discussed above have never reached 50% of pressure demagnetization (Table 3), so using "median destructive stress" - the pressure at which the sample's IRM is reduced by 50% - is not appropriate. Instead, the destructive hydrostatic pressure (DHP), needed to remove 10% (DHP10%) and 20% (DHP20%) of the SIRM is better suited to characterize the pressure demagnetization efficiency of pyrrhotite-bearing samples, and simplifies the comparison of our data with earlier works. DHP10% and DHP20% are presented for all samples in Table 3. The degree of linear correlation of DHP10% and DHP20% with B_{cr} is poor: approximation confidence R^2 = 0.52 for DHP10% and R^2 = 0.55 for DHP20%. If we consider SD and PSD samples separately, the same linear correlation improves: R^2 = 0.7 for DHP10% and R^2 = 0.6 for DHP20%, indicating that domain state may play a role in pressure demagnetization processes as well.

There is no pressure-induced ferrimagnetic-to-paramagnetic transition observed at 2 GPa. This is consistent with the results of Rochette et al. (2003), who demonstrated that such transition occurs at 2.8 GPa.

4.3. Relevance of usage of synthesized analogues for investigating meteorite magnetism

The existence of pyrrhotite-bearing meteorites, such as CM and CV chondrites, R-chondrites, SNC [Rochette et al., 2005; Tikoo et al., 2015; Cournede et al., 2015], justifies the relevance of synthetic samples as analogous to natural meteorite samples. Cournede et al. (2015) recently demonstrated that pyrrhotite is a remanence carrier in CM meteorites. Fu et al. (2014) showed that natural ferrimagnetic sulfides in Allende meteorite (a CV carbonaceous chondrite) exhibit bulk SD/PSD behaviour, but may also contain large (1 to >10 μm) aggregates of many smaller, possibly interacting grains as revealed by SEM investigations. These crystal habits are very similar to our synthesized samples imaged in Fig. 1 and further justify the synthesized samples as being broadly analogous to natural samples of extraterrestrial materials.

4.4. Implications to meteorite paleomagnetism and planetary magnetic anomalies

One may question how our pressure demagnetization results may apply to Earth or Mars where we are more likely to deal with other than IRM types of magnetization: e.g., thermal remanent magnetization (TRM) or shock remanent magnetization (SRM) or a combination of both. Although it was demonstrated by Bezaeva et al. (2010) that SIRM may be more pressure sensitive than TRM, this is not a general result. Instead, we argue that studies of SIRM pressure sensitivity are a first step towards approximating TRM pressure sensitivity of the same material. TRM-based pressure sensitivity studies on pyrrhotite will be more experimentally challenging, as even the slightest oxidation can lead to profound changes in magnetic properties.

It was mentioned in the introduction that SD monoclinic pyrrhotite is one of the main candidate magnetic minerals responsible for carrying the remanence that gives rise to Martian magnetic anomalies. Our pressure demagnetization experiments model possible impact demagnetization of the Martian crust around impact basins in both northern and southern hemispheres, where the crust is demagnetized (likely via an impact shock mechanism). However, acquisition of remanence under pressure may be a more likely scenario for portions of the ancient crust (>4.0 Ga) in the southern hemisphere of Mars, which likely acquired its remanent magnetization at pressure rather than by impact demagnetization. Such a scenario would be better modeled via IRM acquisition experiments at pressure. Conducting such experiments using the same synthesized samples is a part of the motivation for this work.

Our pressure demagnetization results have implications for meteorite paleomagnetism as well. Tikoo et al. (2015) has recently investigated the acquisition of remanence under pressure for an array of meteorites, including pyrrhotite-bearing samples with shock stage >2 GPa (SNC and CMs). For correct paleointensity determinations on such samples, it is important to know the expected demagnetization magnitude, which is likely to take place during impact events. Our pressure demagnetization results provide such an estimate. Not taking into consideration shock demagnetization degree (for which hydrostatic pressure demagnetization degree serves as a first approximation) may lead to underestimation of paleointensities recovered from shocked pyrrhotite-bearing meteorites.

5. Conclusions

(1) We synthesized monoclinic pyrrhotite (Fe_7S_8) using the molten-salt synthesis method. XRD, SEM, Mössbauer and thermomagnetic analyses confirmed the successful synthesis of monoclinic pyrrhotite with a Curie temperature T_c = 593 K, no impurities of hexagonal pyrrhotite, and only minor (~10 mol.%) traces of pyrite. SEM observations revealed pyrrhotite grains in the form of agglomerates predominantly composed of 1–2 μm-sized crystallites, and we therefore refer to our synthesized material as 'non-ideal SD' monoclinic pyrrhotite. The synthesis is reproducible as confirmed by replicate synthesis runs, which produced 'mpo$_2$' and 'mpo$_3$' samples of monoclinic pyrrhotite with similar physical properties.

(2) Hysteresis loops and backfield remanence demagnetization curves show that our samples exhibit predominantly SD behavior with remanence ratios M_{rs}/M_s = 0.53 (powder sample 'mpo$_1$') and 0.58 (dispersed powder sample 'mpo$_1^*$'), bulk coercivities B_c = 35 mT ('mpo$_1$') and 42 mT ('mpo$_1^*$') and remanent coercivities B_{cr} = 41 mT ('mpo$_1$') and 51 mT ('mpo$_1^*$'). FORC diagrams show interacting SD grains and a distribution of microscopic coercivities extending to higher coercivities >100 mT. As our samples have not been crushed and do not contain any hexagonal pyrrhotite impurity, their lower B_c and B_{cr} values (with regard to what was previously published for SD pyrrhotite) better reflect the magnetic properties of pure SD-like monoclinic pyrrhotite.

(3) The materials in this study contain no appreciable concentration of SP grains as shown by the absence of frequency dependence of magnetic susceptibility in the temperature range 5–300 K for frequencies up to 997 Hz and in room temperature data for frequencies up to 15 kHz.

(4) The characteristic low-temperature transition of pyrrhotite known as the Besnus transition is observed at ~33 K, which is in good agreement with previously published data (Rochette et al., 1990)

(5) Application of hydrostatic pressures up to 1.8 and up to 2 GPa using non-magnetic high-pressure cells resulted in demagnetization of the sample's SIRM by 32–38%. Repeated cycling from 1.8 GPa to atmospheric pressure and back resulted in further decrease in remanence and total demagnetization after three pressure cycles of 44%. Decompression from 1.8 GPa as well as from 2 GPa to ambient pressure resulted in further increase up to 19% in residual magnetic remanence, which is consistent with earlier observations on pyrrhotite (Bezaeva et al., 2010).

(6) We have not observed pressure-induced ferrimagnetic-to-paramagnetic transition at 2 GPa.

(7) We have not observed any pressure-induced permanent changes in SIRM or B_{cr} (reflecting the magnetic hardness of the sample) upon decompression from 2 GPa. This indicates that no permanent changes in the magnetic properties took place during pressure cycling, which is consistent with results of Bezaeva et al. (2010) for the 0–1.2 GPa hydrostatic pressure range and Demory et al. (2013) for 0–1.4 GPa hydrostatic pressure range.

(8) Pressure demagnetization results have important implications for meteorite paleomagnetism and suggest that paleointensities of shocked pyrrhotite-bearing meteorites may be underestimated, as their possible shock demagnetization effect was not taken into consideration. Additional experiments of IRM acquisition under pressure will be conducted on the same synthesized samples in the future.

References

Arnold, R.G., 1967. Range in composition and structure of 82 natural terrestrial pyrrhotites. Can. Mineral. 9, 31–50.

Besnus, M.J., Meyer, A.J., 1964. Nouvelles données expérimentales sur le magnétism de la pyrrhotine naturelle. In: Proc. Int. Conf. Magn., Nottingham, pp. 507–511.

Bezaeva, N.S., Rochette, P., Gattacceca, J., Sadykov, R.A., Trukhin, V.I., 2007. Pressure demagnetization of the Martian crust: ground truth from SNC meteorites. Geophys. Res. Lett. 34, L23202. http://dx.doi.org/10.1029/2007GL031501.

Bezaeva, N.S., Gattacceca, J., Rochette, P., Sadykov, R.A., Trukhin, V.I., 2010. Demagnetization of terrestrial and extraterrestrial rocks under hydrostatic pressure up to 1.2 GPa. Phys. Earth Planet. Inter. 179, 7–20. http://dx.doi.org/10.1016/j.pepi.2010.01.004.

Bowles, J., Jackson, M., Chen, A., Solheid, P., 2009. Interpretation of low-temperature data Part 1: Superparamagnetism and paramagnetism. IRM Q. 19 (3), 7–11, 1.

Burov, B.V., Yasonov, P.G., 1979. Introduction into Differential Thermomagnetic Analysis of Rocks. Kazan' State University Press, Kazan, p. 157 (in Russian).

Burov, B.V., Nurgaliev, D.K., Yasonov, P.G., 1986. Paleomagnetic Analysis. Kazan State University Press, Kazan, p. 168 (in Russian).

Chichagov, A.V., Belonozhko, A.B., Lopatin, A.L., Dokina, T.N., Samokhvalova, O.L., Ushakovskaya, T.V., Shilova, Z.V., 1990. Information-calculating system on crystal structure data for minerals (MINCRYST). Kristallografie 35 (3), 610–616 (in Russian) http://database.iem.ac.ru/mincryst/.

Chareev, D.A., Voronin, M.V., Osadchii, E.G., 2014. Thermodynamic study of monoclinic pyrrhotite in equilibrium with pyrite in Ag–Fe–S system by solid-state electrochemical cell technique. Am. Mineral. 99 (10), 2031–2034. http://dx.doi.org/10.2138/am-2014-4753.

Clark, D.A., 1984. Hysteresis properties of sized dispersed monoclinic pyrrhotite grains. Geophys. Res. Lett. 11 (3), 173–176. http://dx.doi.org/10.1029/GL011i003p00173.

Cournede, C., Gattacceca, J., Gounelle, M., Rochette, P., Weiss, B.P., Zanda, B., 2015. An early solar system magnetic field recorded in CM chondrites. Earth Planet. Sci. Lett. 410, 62–74. http://dx.doi.org/10.1016/j.epsl.2014.11.019.

Dekkers, M.J., 1988. Magnetic properties of natural pyrrhotite Part I: Behaviour of initial susceptibility and saturation-magnetization-related rock-magnetic parameters in a grain-size dependent framework. Phys. Earth Planet. Inter. 52, 376–393. http://dx.doi.org/10.1016/0031-9201(88)90129-X.

Dekkers, M.J., 1990. Magnetic monitoring of pyrrhotite alteration during thermal demagnetization. Geophys. Res. Lett. 17, 779–782. http://dx.doi.org/10.1029/GL017i006p00779.

Demory, F., Rochette, P., Gattacceca, J., Gabriel, T., Bezaeva, N.S., 2013. Remanent magnetization and coercivity of rocks under hydrostatic pressure up to 1.4 GPa. Geophys. Res. Lett. 40 (15), 3858–3862. http://dx.doi.org/10.1002/grl.50763.

Dunlop, D.J., Arkani-Hamed, J., 2005. Magnetic minerals in the Martian crust. J. Geophys. Res. 110, E12S04. http://dx.doi.org/10.1029/2005JE002404.

Dunlop, D.J., Özdemir, Ö., 1997. Rock Magnetism, Fundamentals and Frontiers. Cambridge University Press, Cambridge, p. 573.

Egli, R., 2013. VARIFORC: an optimized protocol for the calculation of non-regular first-order reversal curve (FORC) diagrams. Global Planet. Change 110 (C), 302–320. http://dx.doi.org/10.1016/j.gloplacha.2013.08.003.

Evans, B.J., Johnson, R.G., Senftle, F.E., Cecil, C.B., Dulong, F., 1982. The ^{57}Fe Mössbauer parameters of pyrite and marcasite with different provenances. Geochim. Cosmochim. Acta 46, 761–775.

Feinberg, J.M., Solheid, P.A., Swanson-Hysell, N.L., Jackson, M., Bowles, J.A., 2015. Full vector low-temperature magnetic measurements of geologic materials. Geochem. Geophys. Geosyst. 16 (1), 301–314. http://dx.doi.org/10.1002/2014GC005591.

Fu, R.R., Lima, E.A., Weiss, B.P., 2014. No nebula magnetization in the Allende CV carbonaceous chondrite. Earth Planet. Sci. Lett. 404, 54–66. http://dx.doi.org/10.1016/j.epsl.2014.07.014.

Gilder, S.A., Egli, R., Hochleitner, R., Roud, S.C., Volk, M.W., Le Goff, M., de Wit, M., 2011. Anatomy of a pressure-induced, ferromagnetic-to-paramagnetic transition in pyrrhotite: Implications for the formation pressure of diamonds. J. Geophys. Res. 116, B10101. http://dx.doi.org/10.1029/2011JB008292.

Gosselin, J.R., Townsend, M.G., Tremblay, R.J., Webster, A.H., 1975. Mössbauer investigation of synthetic single crystal monoclinic Fe$_7$S$_8$. Mater. Res. Bull. 10, 41–50.

Harrison, R.J., Feinberg, J.M., 2008. FORCinel: an improved algorithm for calculating first-order reversal curve (FORC) distributions using locally-weighted regression smoothing. Geochem. Geophys. Geosyst. 9 (5), Q05016. http://dx.doi.org/10.1029/2008GC001987.

Kirichenko, A.S., Kornilov, A.V., Pudalov, V.M., 2005. Properties of polyethylsiloxane as a pressure-transmitting medium. Instr. Exp. Tech. 48 (6), 813–816. http://dx.doi.org/10.1007/s10786-005-0144-5.

Kissin, S.A., Scott, S.D., 1982. Phase relations involving pyrrhotite below 350°C. Econ. Geol. 77, 1739–1754. http://dx.doi.org/10.2113/gsecongeo.77.7.1739.

Langlais, B., Purucker, M.E., Mandea, M., 2004. Crustal magnetic fields of Mars. J. Geophys. Res. 109, E02008. http://dx.doi.org/10.1029/2003JE002048.

Louzada, K.L., Stewart, S.T., Weiss, B.P., Gattacceca, J., Bezaeva, N.S., 2010. Shock and static pressure demagnetization of pyrrhotite and implications for the Martian crust. Earth Planet. Sci. Lett. 290, 90–101. http://dx.doi.org/10.1016/j.epsl.2009.12.006.

Menyeh, A., O'Reilly, W., 1996. Thermoremanent magnetization in monodomain monoclinic pyrrhotite Fe$_7$S$_8$. J. Geophys. Res. 101 (B11), 25045–25051. http://dx.doi.org/10.1029/96JB01188.

Menyeh, A., O'Reilly, W., 1997. Magnetic hysteresis properties of fine particles of monoclinic pyrrhotite Fe$_7$S$_8$. J. Geomagn. Geoelec. 49, 965–976.

Menyeh, A., O'Reilly, W., 1998. Thermoremanence in monoclinic pyrrhotite particles containing few domains. Geophys. Res. Lett. 25 (18), 3461–3464. http://dx.doi.org/10.1029/98GL02220.

Moh, G.H., Taylor, L.A., 1971. Laboratory techniques in experimental sulfide petrology. Neues Jahrb. Mineral. Monatsh. 10, 450–459.

Narazawa, H., Morimoto, N., 1971. Phase relations and superstructures of pyrrhotite, Fe$_{1-x}$S. Mater. Res. Bull. 6, 345–357. http://dx.doi.org/10.1016/0025-5408(71)90168-1.

O'Reilly, W., Hoffmann, V., Chouker, A.C., Soffel, H.C., Menyeh, A., 2000. Magnetic properties of synthetic analogues of pyrrhotite ore in the grain size range 1–24 μm. Geophys. J. Int. 142, 669–683. http://dx.doi.org/10.1046/j.1365-246x.2000.00169.x.

Roberts, A.P., Pike, C.R., Verosub, K.L., 2000. First-order reversal curve diagrams: a new tool for characterizing the magnetic properties of natural samples. J. Geophys. Res. 105 (B12), 28461–28475. http://dx.doi.org/10.1029/2000JB900326.

Rochette, P., Fillon, G., Mattei, J.-L., Dekkers, M.J., 1990. Magnetic transition at 30–34 Kelvin in pyrrhotite: insight into a widespread occurrence of this mineral in rocks. Earth Planet. Sci. Lett. 98, 319–328. http://dx.doi.org/10.1016/0012-821X(90)90034-U.

Rochette, P., Fillon, G., Ballou, R., Brunet, F., Ouladdiaf, B., Hood, L., 2003. High pressure magnetic transition in pyrrhotite and impact demagnetization on Mars. Geophys. Res. Lett. 30 (13), 1683. http://dx.doi.org/10.1029/2003GL017359.

Rochette, P., Gattacceca, J., Chevrier, V., Hoffmann, V., Lorand, J.-P., Funaki, M., Hochleitner, R., 2005. Matching Martian crustal magnetization and magnetic properties of Martian meteorites. Meteorit. Planet. Sci. 40, 529–540.

Rochette, P., Fillon, G., Dekkers, M.J., 2011. Interpretation of low-temperature data Part 4: The low-temperature magnetic transition of monoclinic pyrrhotite. IRM Q. 21 (1), 7–11, 1.

Sadykov, R.A., Bezaeva, N.S., Kharkovskiy, A.I., Rochette, P., Gattacceca, J., Trukhin, V. I., 2008. Nonmagnetic high pressure cell for magnetic remanence measurements up to 1.5 GPa in a superconducting quantum interference device magnetometer. Rev. Sci. Instrum. 79, 115102. http://dx.doi.org/10.1063/1.2999578.

Sassen, R., McCabe, C., Kyle, J.R., Chinn, E.W., 1989. Deposition of magnetic pyrrhotite during alteration of crude oil and reduction of sulfate. Org. Geochem. 14 (4), 381–392. http://dx.doi.org/10.1016/0146-6380(89)90004-1.

Soffel, H.C., 1977. Pseudo-single-domain effects and single-domain multidomain transition in natural pyrrhotite deduced from domain structure observations. J. Geophys. 42, 351–359.

Soffel, H.C., 1981. Domain structure of natural fine-grained pyrrhotite in a rock matrix (diabase). Phys. Earth Planet. Inter. 26, 98–106. http://dx.doi.org/10.1016/0031-9201(81)90102-3.

Schwarz, E., Vaughan, D., 1972. Magnetic phase relations of pyrrhotite. J. Geomagn. Geoelec. 24, 441–458. http://dx.doi.org/10.5636/jgg.24.441.

Tikoo, S.M., Gattacceca, J., Swanson-Hysell, N.L., Weiss, B.P., Suavet, C., Cournede, C., 2015. Preservation and detectability of shock-induced magnetization. J. Geophys. Res. Planets 120 (9), 1461–1475. http://dx.doi.org/10.1002/2015JE004840.

Wehland, F., Stancu, A., Rochette, P., Dekkers, M.J., Appel, E., 2005. Experimental evaluation of magnetic interaction in pyrrhotite-bearing samples. Phys. Earth Planet. Inter. 153, 181–190. http://dx.doi.org/10.1016/j.pepi.2005.05.006.

Wolfers, P., Fillon, G., Ouladdiaf, B., Ballou, R., Rochette, P., 2011. The pyrrhotite 32 K magnetic transition. Solid State Phenom. 170, 174–179. http://dx.doi.org/10.4028/www.scientific.net/SSP.170.174.

Worm, H.U., Clark, D., Dekkers, M.J., 1993. Magnetic susceptibility of pyrrhotite: grain size, field and frequency dependence. Geophys. J. Int. 114, 127–137.